RSC Advances

PAPER

View Article Online
View Journal | View Issue

Cite this: *RSC Adv.*, 2026, **16**, 8517

Fe-doping-driven enhancement of electronic conductivity and electrocatalytic performance in Gd_2O_3 nanoparticles for ultrasensitive electrochemical detection of chloramphenicol in pharmaceutical and milk samples

Tuan-Anh Nguyen, *[af] Nguyen Huu An Nguyen,[b] Ngo Xuan Dinh, [a] Le Thi Thanh Tam, [cd] Nguyen Xuan Quang,[e] Le Trong Lu, [cd] Manh-Huong Phan [fg] and Anh-Tuan Le *[a]

In this study, Gd_2O_3 and Fe-doped Gd_2O_3 NPs were synthesized *via* a thermal decomposition method and integrated into an electrochemical sensing platform to systematically investigate the impact of Fe doping on the electronic conductivity and electrocatalytic performance toward sensitive chloramphenicol (CAP) detection. The structural, morphological, and compositional properties of the Gd_2O_3 and Fe-doped Gd_2O_3 NPs were characterized using FE-SEM, TEM, and VSM techniques. Fe doping significantly enhances the electrical conductivity and the electrochemically active surface area, which was confirmed by cyclic voltammetry (CV) and electrochemical impedance spectroscopy (EIS) measurements. Fe-doped Gd_2O_3 exhibits improved electrocatalytic activity, significantly lowering the activation energy for the CAP electrochemical reduction reaction, as evidenced by linear sweep voltammetry (LSV) and chronoamperometry (CA) measurements. Owing to the aforementioned synergistic contributions, the Fe-doped Gd_2O_3-based electrochemical nanosensor demonstrated remarkable analytical performance in a wide dynamic concentration range with a high electrochemical sensitivity of 1.010 μA μM^{-1} cm^{-2}, a low detection limit of 0.25 μM, excellent repeatability, strong anti-interference ability, and good storage stability. The Fe-doped Gd_2O_3 demonstrated strong potential for CAP detection in pharmaceutical formulations and milk samples with a recovery ranging from 94.1 to 114.0%. The results suggested that the Fe-doped Gd_2O_3 NPs hold great potential for the development of an on-site and point-of-care analytical device for pharmaceutical quality control and antibiotic residue detection in food products.

Received 22nd November 2025
Accepted 6th February 2026

DOI: 10.1039/d5ra09035k

rsc.li/rsc-advances

1. Introduction

In recent years, the rapid development of analytical technologies and nanotechnology has led to significant advances in various sensing nanoplatforms.[1–3] Among these, electrochemical sensors have gained considerable attention due to their high sensitivity, cost-effectiveness, portability, simplicity and rapid detection capability.[3–5] These characteristics make electrochemical sensors especially suitable for applications demanding real-time and point-of care diagnostics, particularly in environmental monitoring, pharmaceutical quality control and medical diagnostics, as well as food and beverage safety and quality assurance.[2,4,6] Fundamentally, the sensing performance of an electrochemical nanosensor originates from the physicochemical characteristic of the electrode materials – namely, its electronic conductivity, electrocatalytic activity, and adsorption/diffusion capacity at the electrode–electrolyte interface.[7–9] First, electronic conductivity plays a pivotal role in determining the electron transfer kinetics within the sensor system. A highly conductive electrode nanomaterial facilitates the rapid movement of charge carriers, and accelerates the electrochemical reactions, thereby enhancing the responsiveness and sensitivity.[8] Second, electrocatalytic activity governs the material's ability to accelerate the kinetics of analyte

[a]*Phenikaa University Nano Institute (PHENA), Phenikaa School of Engineering (PSE), Phenikaa University, Hanoi, Vietnam. E-mail: anh.nguyentuan1@phenikaa-uni.edu.vn; tuan.leanh@phenikaa-uni.edu.vn*

[b]*SenTia School, 19 To Huu, Nam Tu Liem, Ha Noi, Vietnam*

[c]*Graduate University of Science and Technology, Vietnam Academy of Science and Technology, 18 Hoang Quoc Viet, Hanoi, Vietnam*

[d]*Institute for Materials Science, Vietnam Academy of Science and Technology, 18 Hoang Quoc Viet, Hanoi, Vietnam*

[e]*University of Transport Technology, Trieu Khuc, Thanh Xuan District, Hanoi, Vietnam*

[f]*Department of Physics, University of South Florida, Tampa, Florida, 33620, USA*

[g]*Center for Materials Innovation and Technology (CMIT), VinUniversity, Hanoi, Vietnam*

oxidation or reduction at the electrode–electrolyte interface by lowering the activation energy barriers, thus enabling the detection of analytes at lower concentrations and under milder conditions.[10] Third, effective adsorption/diffusion capacity ensures efficient transport and retention of target molecules at the electroactive sites on the electrode surface, thereby enhancing analyte accessibility and improving analytical performance.[11] Therefore, substantial research efforts have focused on the engineering of novel electrode materials with finely tuned electronic conductivity, electrocatalytic activity, and adsorption/diffusion capacity, achieved through strategies such as surface modification, doping, nanostructuring, and compositional tuning.

Nanostructured materials, particularly metal oxides, have demonstrated tremendous promise for electrode modification due to their high surface area, tunable electronic properties, and chemical stability.[8,12] Among these, rare-earth oxides (RE_2O_3) such as gadolinium oxide (Gd_2O_3) exhibit promising attributes for sensor applications due to their unique electronic structure, tunable electric conductivity, and unusual 4f sub-shell electronic and chemical performance.[13,14] Nevertheless, due to its wide band gap and limited charge carrier population, the low intrinsic electronic conductivity of pristine Gd_2O_3 remains a major limitation that hinders its widespread use in high-performance electrochemical sensing platforms.[15] Furthermore, the electrocatalytic performance of bulk Gd_2O_3 is limited by particle agglomeration and disordered stacking, which significantly reduces the number of exposed active sites.[13] To overcome these shortcomings, doping strategies have been employed to modulate the structural, electronic, and catalytic properties of Gd_2O_3. Among the various potential dopants, iron (Fe) has emerged as a particularly promising candidate due to its high electrical conductivity (1.00×10^7 S m^{-1} at 20 °C), low resistivity (1×10^{-7} Ω m), and a high density of free electrons (17×10^{28} electrons per m^3), and rich redox chemistry (Fe^{2+}/Fe^{3+}).[16] Fe-doping has proven to be an effective strategy for enhancing the electrochemical activity and analytical sensing performance of various metal oxides.[16–18] For example, Fe-doped WO_3 exhibited significant improvements in curcumin detection due to enhanced electron transfer and catalytic reactivity, offering a linear detection range (5 μM to 60 μM) and a low limit of detection (6.2×10^{-8} M).[19] Lavanva *et al.* fabricated a novel disposable screen-printed carbon electrode modified by Fe doped SnO_2 nanoparticles (NPs) for carbamazepine detection in pharmaceutical products. The Fe-doped SnO_2 NPs deliver a large effective electrode surface area and high electron conductivity, resulting in fast and sensitive current response to CBZ over a wide linear range of 0.5–100 μM with a low detection limit of 92 nM.[20] These results collectively affirm the potential of Fe doping as an effective strategy to improve the electrochemical performance of Fe-doped metal oxide-based electrochemical sensors. Therefore, the incorporation of Fe into Gd_2O_3 NPs is expected to enhance electronic conductivity by increasing charge carrier density and mobility, primarily through donor level formation and bandgap narrowing. Additionally, it mitigates particle agglomeration, exposing more accessible active sites for electrochemical reactions and thereby improving overall electrocatalytic performance.

Antibiotics have long been considered revolutionary in the treatment of infectious diseases in both humans and livestock. They play a crucial role in controlling bacterial infections, improving animal health, and increasing productivity in the livestock industry.[21] However, the overuse and misuse of antibiotics in livestock farming – whether for disease prevention, treatment, or growth promotion have raised serious food safety and public health concerns.[22] Alongside growing concerns about antibiotic residues in food products, the quality control of pharmaceutical products containing antibiotics has become increasingly critical.[23] Inconsistencies in active ingredient concentrations, the presence of impurities or degradation products in drug formulations can significantly undermine therapeutic effectiveness and elevate toxicity risks.[23,24] Chloramphenicol (CAP), a broad-spectrum phenolic antibiotic, is particularly concerning due to its tendency to accumulate in the human body. CAP has been associated with severe adverse health effects, including aplastic anemia, gray baby syndrome, and bone marrow suppression.[25,26] Consequently, the use of CAP in food-producing animals has been strictly prohibited in the European Union, the United States, and many other countries.[27,28] Despite these restrictions, CAP remains widely used in certain regions due to its cost-effectiveness and strong antibacterial properties. Furthermore, rigorous quality control of CAP in pharmaceutical formulations is imperative to ensure that pharmaceuticals meet established safety, efficacy, and purity standards. Therefore, given the potential health risks associated with CAP contamination, there is an urgent need for rapid, reliable, robust, and highly sensitive detection platforms to ensure food safety, protect public health, and support regulatory enforcement.

In this study, we present the synthesis of undoped Gd_2O_3 NPs and Fe-doped Gd_2O_3 NPs as active electrode modifiers for the electrochemical detection of CAP. By systematically comparing the electrochemical characteristics in redox probe $[Fe(CN)_6]^{3-/4-}$ and the electrochemical behavior in CAP analyte of the bare SPE, undoped Gd_2O_3-, and Fe-doped Gd_2O_3-modified screen-printed carbon electrode (SPE), the results showed that the Fe doping improved the electrochemical properties of the undoped Gd_2O_3 NPs by increasing its electrical conductivity and electrocatalytic response. As a result, the Fe-doped Gd_2O_3/SPE demonstrated excellent analytical sensing performance towards CAP sensing over a wide linear range with high electrochemical sensitivity and low detection limit. The repeatability, anti-interference ability, storage stability, and practical applicability for the detection of CAP in pharmaceutical formulations and milk samples of the proposed sensor were also investigated. The findings of this study are expected not only to provide valuable insight into dopant-modified rare-earth oxides for electrochemical sensing nanoplatforms but also to contribute to the development of a new class of high-performance, cost-effective, sensitive, and portable electrochemical sensors for monitoring antibiotic residues in food samples and pharmaceutical quality control.

2. Experimental section

2.1. Chemicals

Iron(III) acetylacetonate ($Fe(acac)_3$, 99.9%), gadolinium(III) acetate hydrate ($Gd(Ac)_3$, 99.9%), 1-octadecanol (OCD-ol, 95%),

oleic acid (OA, 90%), oleyamine (OM, 70%), 1-octadecene (ODE, 90%), absolute ethanol and *n*-hexane were purchased from Sigma-Aldrich, Germany. Potassium ferricyanide ($K_3Fe(CN)_6$), potassium ferrocyanide ($K_4Fe(CN)_6$), potassium chloride (KCl), potassium dihydrogen phosphate (KH_2PO_4), sodium chloride (NaCl), and dibasic sodium phosphate (Na_2HPO_4) were manufactured by Merck KGaA, Germany. Chloramphenicol (CAP > 98%) was supplied by Sigma-Aldrich, Germany. All the chemicals and reagents employed in this study were analytical grade and used without additional refinement.

2.2. Synthesis of Gd_2O_3 and Fe-doped Gd_2O_3 NPs and fabrication of modified electrodes

The Gd_2O_3 and Fe-doped Gd_2O_3 NPs were synthesized *via* a thermal decomposition method following our previously reported work.[29] Briefly, 10 mmol gadolinium(III) acetate (for the synthesis of Gd_2O_3 NPs), 9 mmol gadolinium(III) acetate and 1 mmol iron(III) acetylacetonate (for the synthesis of Fe-doped Gd_2O_3 NPs) were introduced into a 100 mL three-neck round-bottom flask containing a pre-prepared solution of oleic acid (OA) and oleylamine (OM) in a 2 : 1 molar ratio, along with 40 mL of octadecene as the solvent. The reaction mixture was stirred at 100 °C for 1 h until the precursors completely dissolved. Subsequently, the temperature increased to 200 °C and maintained for 3 h, followed by further heating to 320 °C for 2 h. The entire reaction was carried out under a continuous flow of nitrogen gas. After the reaction, the reaction mixture was allowed to cool to room temperature, and the resulting products were isolated by centrifugation, washed four times with absolute ethanol. The Gd_2O_3 and Fe-doped Gd_2O_3 NPs was collected and dried under vacuum at 70 °C.

For electrode modification, the bare SPE was thoroughly rinsed with ethanol and distilled water to remove impurities, giving a smooth and shiny surface. The Gd_2O_3 and Fe-doped Gd_2O_3 suspensions were prepared by dispersing 1 mg Gd_2O_3 and Fe-doped Gd_2O_3 powder in 1 mL *n*-hexane and subjected to 1 h of ultrasonication. Next, 8 μL of the above suspensions were dropped cast onto the working electrode of the bare SPE and allowed to dry at room temperature. Finally, the Gd_2O_3/SPE and Fe-doped Gd_2O_3/SPE were stored at room temperature for subsequent electrochemical experiments.

2.3. Instrumentation

The surface morphological features of samples were scrutinized by FE-SEM (field emission scanning electron microscopy FE-SEM, S-4800). The presence of Fe in Fe-doped Gd_2O_3 sample was confirmed by transmission electron microscopy (TEM), vibrating sample magnetometry (VSM), and X-ray Photoelectron Spectroscopy (XPS) techniques. Electrochemical investigations were conducted on A PalmSens 4.0 Potentiostat/Galvanostat/Impedance Analyzer workstation potentiostat (PalmSens Compact Electrochemical Interfaces, Netherlands).

2.4. Electrochemical measurements

Cyclic voltammetry (CV), differential pulse voltammetry (DPV), linear sweep voltammetry (LSV) chronoamperometry (CA), and electrochemical impedance spectroscopy (EIS) techniques were used to study the electrochemical characteristics and electrochemical behaviors toward CAP of the bare SPE, Gd_2O_3/SPE and Fe-doped Gd_2O_3/SPE. The electrochemical characteristics of the unmodified and modified SPE electrodes were studied by CV and EIS techniques in 0.1 M KCl solution containing 2.5 mM benchmark redox probe $[Fe(CN)_6]^{3-/4-}$. CV measurements were applied with a potential window between −0.25 and 0.5 V with scan rate in the range of 10 to 60 mV s^{-1}. EIS measurements were carried out in a frequency range between 100 000 Hz to 0.01 Hz. The electrochemical behaviors and electrocatalytic activity of CAP on the unmodified and modified SPE electrodes were investigated by CV, LSV, CA, and DPV techniques in an aqueous phosphate buffer electrolyte solution (0.1 M PBS). CV technique was carried out with a potential window between −1.0 and −0.3 V with scan rate in the range of 10 to 60 mV s^{-1}. LSV measurement was recorded by scan potential from −0.1 to −1.0 V with $E_{step} = 0.01$ V and $t_{equilibration} = 120$ s. CA measurement was performed at the potential of −750 mV in the absence and presence of 50 μM CAP with $t_{intervals}$ of 0.06 s and $t_{running}$ of 5 s. DPV technique was performed in the potential range from −0.35 to −0.9 V at a scan rate of 6 mV s^{-1} with $E_{pulse} = 0.075$ V, and $t_{pulse} = 0.2$ s.

2.5. Real samples preparation

Commercial pharmaceutical tablets containing 500 mg of CAP were purchased from a local drug store in Hanoi, Vietnam. For the electrochemical analysis of the pharmaceutical formulation, five tablets were accurately weighed and finely pulverized. Then, 50 mg of the homogenized powder was dissolved in 50 mL 0.1 M PBS (pH 7.0), stirred for 3 h to ensure that tablets were dissolved completely, and filtered through Whatman filter paper. To obtain final CAP concentrations in the working range, appropriate aliquots of the clear supernatant liquid were diluted with 0.1 M PBS (pH 7.0).

Milk samples were purchased from the local supermarket. To prepare milk samples, 1 mL of milk was diluted 5 mL of 0.1 M PBS (pH 7.0) and the resulting solution was mixed completely by a vortex mixer and centrifuged for 5 min and filtered through Whatman filter paper. Finally, obtained sample was spiked with certain amounts of CAP standard solution (25, 50, and 100 μM). The actual concentrations of CAP in commercial pharmaceutical tablets and milk samples were calculated by using three repeated DPV measurements and the regression equation of the calibration curve.

3. Results and discussion

3.1. Physicochemical characteristics of Gd_2O_3 and Fe-doped Gd_2O_3 NPs

The surface morphology of the undoped Gd_2O_3 and Fe-doped Gd_2O_3 samples was investigated using FE-SEM technique at different magnifications. The FE-SEM images obtained at magnifications of 20.0k and 100k (Fig. 1a and b) demonstrate that the undoped Gd_2O_3 sample exhibits a relatively uniform and aggregated porous micromorphology, which is composed

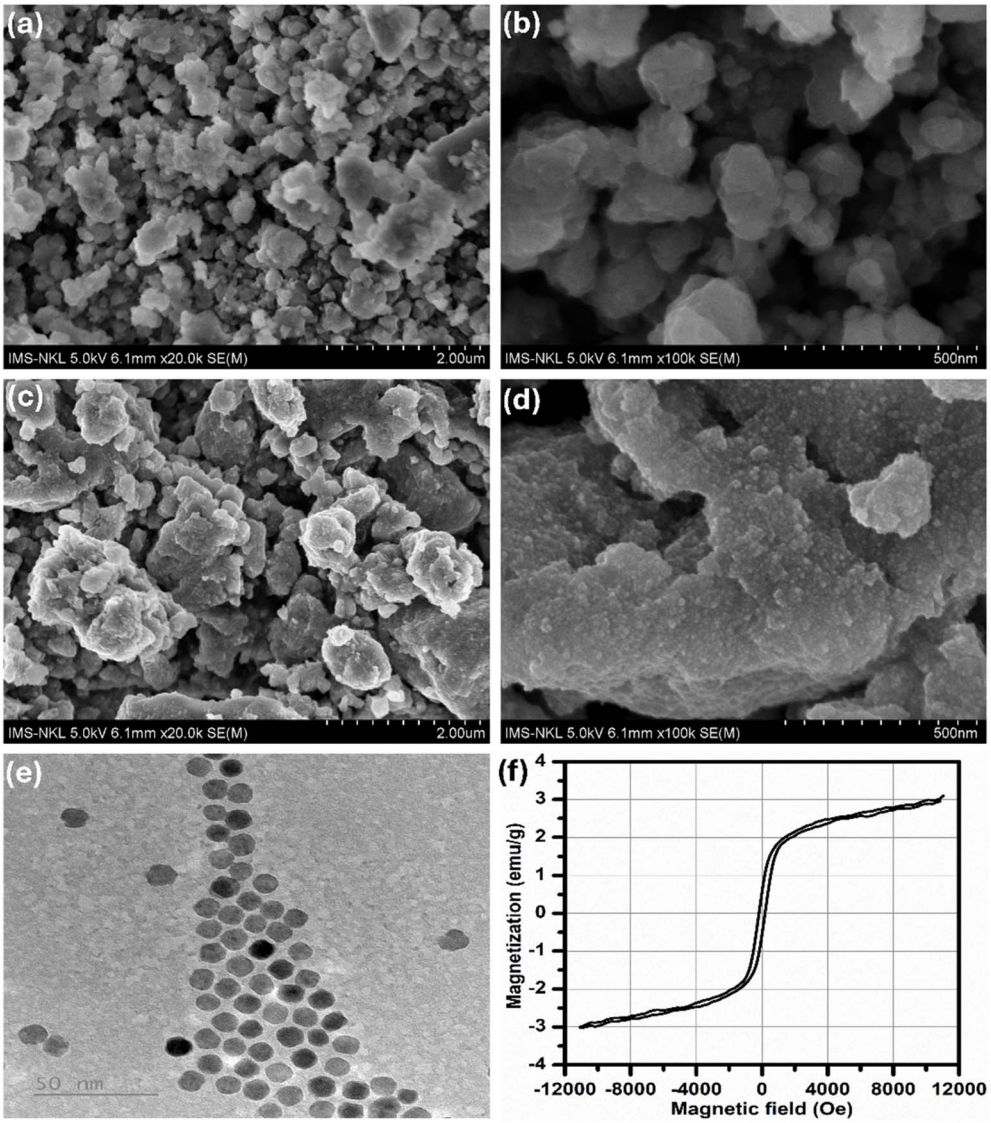

Fig. 1 SEM images at different magnification of Gd_2O_3 (a and b) and Fe–Gd_2O_3 NPs (c and d). TEM image (e) and magnetic hysteresis loop (f) of Fe–Gd_2O_3 NPs.

of well-agglomerated NPs with clean and smooth surface features. Upon Fe doping, the particles tend to form larger agglomerates with rougher surfaces compared to the undoped Gd_2O_3 NPs (Fig. 1c). At higher magnification (Fig. 1d), it is clear that the Fe-doped Gd_2O_3 sample displays a porous, network-like micromorphology, in which small, fine primary Fe-doped Gd_2O_3 NPs are interconnected, forming a continuous and closely packed structure. Full information about the XRD pattern, UV-Vis spectrum, and Gd/Fe molar ratio measured by ICP-MS was reported in our previous study.[29]

TEM analysis was carried out to examine the morphology of the Fe-doped Gd_2O_3 NPs. As shown in Fig. 1e, the particles exhibit good sphericity and a relatively uniform size distribution, with an average diameter of less than 20 nm. The presence of Fe doping in Gd_2O_3 NPs was further investigated using VSM technique, and the corresponding hysteresis loop is presented in Fig. 1f. The Fe-doped Gd_2O_3 NPs exhibits a distinct hysteresis loop with a saturation magnetization (M_s) of approximately 2 emu g^{-1}. While pristine Gd_2O_3 is inherently non-magnetic, this enhancement in magnetic response can be attributed to the presence of Fe ions, which introduce four unpaired electrons (Fe = [Ar] $4s^2$ $5d^6$) in its 3d orbitals and promote magnetic exchange interactions.[30,31]

XPS analysis was performed to elucidate the surface elemental composition as well as the oxidation states and lattice incorporation of Fe species in the Fe-doped Gd_2O_3 NPs. The survey spectrum presented in Fig. 2a shows five predominant peaks corresponding to Gd 4d, C 1s, O 1s, Fe 2p, and Gd 3d, thereby verifying the elemental composition of the Fe-doped Gd_2O_3 NPs and its agreement with the precursor composition. The Gd 4d high-resolution spectrum (Fig. 2b) displays two characteristic peaks at binding energies of 140.2 eV and 146.4 eV, which are ascribed to the Gd $4d_{5/2}$ and Gd $4d_{3/2}$ spin-orbits split doublet, respectively.[32] Furthermore, the presence of

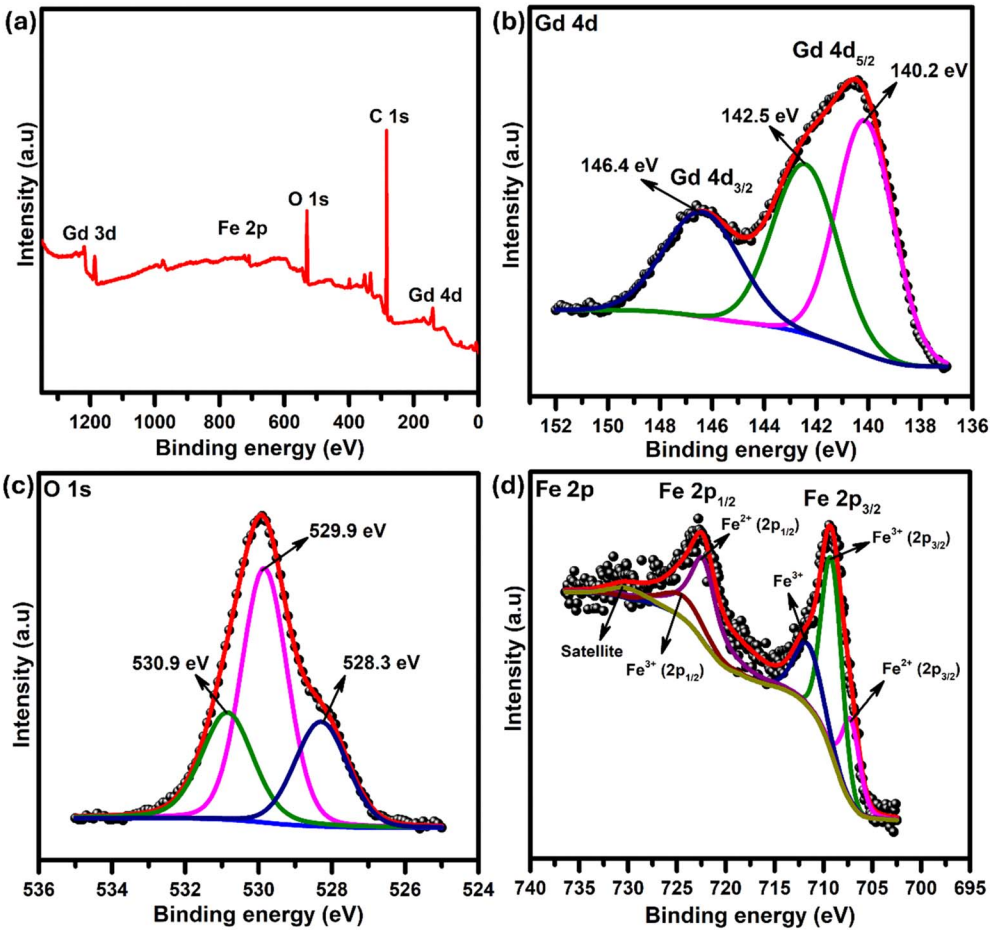

Fig. 2 Scan survey XPS spectrum of the Fe-doped Gd_2O_3 NPs (a) and high-resolution XPS spectra of Gd 4d (b), O 1s (c), and Fe 2p (d).

a satellite peak at binding energy of 142.5 eV suggests interactions between the Gd 4d core levels and partially filled 4f orbitals, thereby confirming the preservation of the intrinsic electronic structure of Gd^{3+} after Fe doping in the as-synthesized Fe-doped Gd_2O_3 NPs.[33,34] The high-resolution spectrum of the O 1s shows the three deconvoluted peaks at 528.3, 529.9, and 530.9 eV (Fig. 2c). The dominant O 1s peak located at 529.9 eV can be attributed to lattice oxygen in Gd–O species, further indicating the formation of Gd_2O_3.[35] Two shoulder peaks at 528.3 and 530.9 eV are associated with oxygen species in the carbonyl (C=O) and carboxyl group (–COOH) originating from terminating groups of the oleic acid. The high-resolution Fe 2p spectrum exhibits well-defined doublet peaks corresponding to the spin–orbit components Fe $2p_{3/2}$ and Fe $2p_{1/2}$[36,37] (Fig. 2d). The deconvoluted Fe $2p_{3/2}$ spectrum exhibits three peaks at binding energies of 707.4, 709.3, and 711.9 eV, which are attributed to the Fe^{2+} octahedral species, Fe^{3+} octahedral species, and the satellite of Fe^3, respectively.[37–39] Similarly, the Fe $2p_{1/2}$ spectrum exhibits peaks at 722.6, 725.2, and 730.6 eV, corresponding to Fe^{2+} octahedral species, Fe^{3+} octahedral species, and the satellite of Fe^{3+}, respectively.[39,40] The XPS analysis suggests that Fe in the doped Gd_2O_3 lattice occupies octahedral sites in both Fe^{2+} and Fe^{3+} oxidation states.

3.2. Electrochemical characterizations of the bare SPE and Gd_2O_3-, Fe-doped Gd_2O_3-modified SPE electrodes

To better understand the electrochemical redox behavior and electrocatalytic activity of bare SPE, Gd_2O_3/SPE, and Fe-doped Gd_2O_3/SPE, cyclic voltammetry (CV) and electrochemical impedance spectroscopy (EIS) were performed in a 0.1 M KCl solution containing 2.5 mM $[Fe(CN)_6]^{3-/4-}$ as a redox probe. As illustrated in Fig. 3a, all electrodes, both modified and unmodified, exhibited well-defined, reversible redox peaks associated with the $[Fe(CN)_6]^{3-/4-}$ redox couple. The nearly rectangular CV profiles, along with the presence of reversible peaks, indicate a combination of pseudocapacitive behavior and double-layer capacitance, suggesting efficient redox processes occurring at the electrode–electrolyte interface. A comparative analysis of the voltammograms (Fig. 3b) reveals a clear trend of increasing oxidation and reduction peak currents (ΔI_{pa} and ΔI_{pc}) from bare SPE to Gd_2O_3/SPE, and further to Fe-doped Gd_2O_3/SPE. The bare SPE electrode showed ΔI_{pa} and ΔI_{pc} values of 56.6 μA and 51.2 μA, respectively. Upon modification with Gd_2O_3, these values increased to 77.0 μA and 77.2 μA, representing enhancements of approximately 36.04% and 50.78%. The incorporation of Fe into Gd_2O_3 NPs resulted in further improvements, with ΔI_{pa} and ΔI_{pc} reaching 81.2 μA and

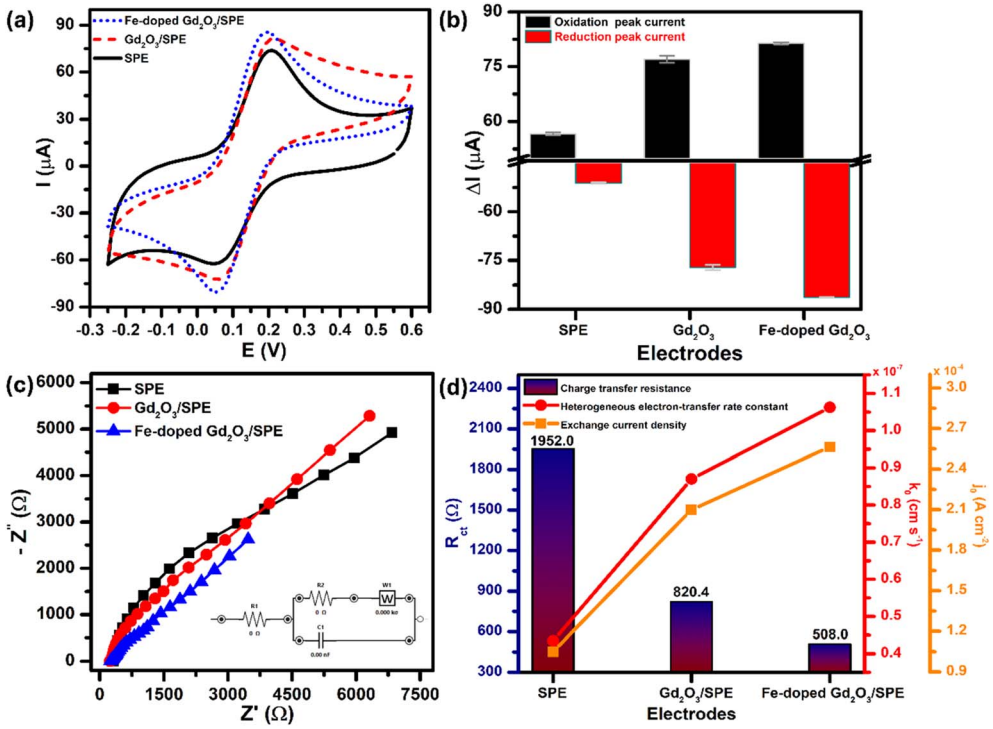

Fig. 3 (a) CV voltammograms and (b) the corresponding bar chart diagram of the anodic/cathodic peak currents of the bare SPE, Gd_2O_3/SPE, and Fe-doped Gd_2O_3/SPE in 2.5 mM $[Fe(CN)_6]^{3-/4-}$ solution containing 0.1 M KCl; (c) Nyquist plots and (d) the corresponding bar chart diagram of charge-transfer resistance (R_{ct}), the heterogeneous electron-transfer rate constants (k_0) and the exchange current density (j_0) values of the bare SPE, Gd_2O_3/SPE, and Fe-doped Gd_2O_3/SPE in 2.5 mM $[Fe(CN)_6]^{3-/4-}$ solution containing 0.1 M KCl. Inset the diagram of Randles equivalent circuit model.

86.4 μA, respectively. Compared to the bare SPE, this corresponds to increases of around 43.46% and 68.75%. These results highlight a progressive enhancement in redox activity due to Fe doping, positioning Fe-doped Gd_2O_3/SPE as the most electrochemically active electrodes among the three investigated electrodes.

To provide additional evidence of the intrinsic electrocatalytic enhancement achieved by doping Gd_2O_3/SPE with Fe, the electrochemically active surface area (ECSA) was evaluated. Fig. S1(a–c) illustrates the CV profiles of bare SPE, Gd_2O_3/SPE, and Fe-doped Gd_2O_3/SPE recorded in a 0.1 M KCl electrolyte containing 2.5 mM $[Fe(CN)_6]^{3-/4-}$, at varying scan rates from 10 to 60 mV s^{-1}, respectively. The corresponding plots of anodic and cathodic peak currents *versus* the square root of the scan rate exhibit strong linearity for all electrodes. As the scan rate increased, the anodic peak current (ΔI_{pa}) showed a consistent rise, whereas the cathodic peak current (ΔI_{pc}) exhibited a decreasing trend for all electrodes. Importantly, the strong linear relationship between peak current and the square root of the scan rate confirms that the redox reactions occurring at the electrode surfaces are governed by a diffusion-controlled mechanism.[5,41] The corresponding linear regression equations are given as follows:

For SPE: $\Delta I_{pa}\ (\mu A) = 220.9v^{1/2}\ (V\ s^{-1}) + 3.2/R^2 = 0.999$

$\Delta I_{pc}\ (\mu A) = -215.2v^{1/2}\ (V\ s^{-1}) + 1.1/R^2 = 0.999$

For Gd_2O_3/SPE:

$\Delta I_{pa}\ (\mu A) = 220.9v^{1/2}\ (V\ s^{-1}) + 22.4/R^2 = 0.996$

$\Delta I_{pc}\ (\mu A) = -255.8v^{1/2}\ (V\ s^{-1}) - 17.3/R^2 = 0.997$

For Fe-doped Gd_2O_3/SPE:

$\Delta I_{pa}\ (\mu A) = 306.8v^{1/2}\ (V\ s^{-1}) + 7.0/R^2 = 0.999$

$\Delta I_{pc}\ (\mu A) = -338.3v^{1/2}\ (V\ s^{-1}) - 3.3/R^2 = 0.999$

The electroactive surface area (EASA) was calculated using the Randles–Sevcik equation, which is detailed below:[42] $I_p = 2.69 \times 10^5\ An^{3/2}D^{1/2}Cv^{1/2}$. This equation relates the peak current (I_p) to the number of electrons transferred (n), the diffusion coefficient (D), the concentration of redox $[Fe(CN)_6]^{3-/4-}$ species (C), and the scan rate (v). In this study, ECSA was estimated using $n = 1$, $D = 6.5 \times 10^{-6}$ cm^2 s^{-1}, and $C = 2.5$ mM. Based on this approach, the calculated ECSA values revealed that Fe-doped Gd_2O_3/SPE (0.197 cm^2) had a larger electroactive surface area than both Gd_2O_3/SPE (0.149 cm^2) and bare SPE (0.126 cm^2). This enhancement is attributed to favorable changes in the crystal structure and phase composition induced by Fe incorporation, which likely facilitates improved electron transportation and more accessible active sites. Generally, a larger electroactive surface area corresponds to better electrocatalytic performance,[43,44] thereby confirming the superior electrocatalytic activity of the Fe-doped Gd_2O_3-modified electrode.

EIS measurements were employed to analyze the charge transfer resistance (R_{ct}), heterogeneous electron transfer rate constant (k^0), and exchange current density (j_0). These parameters will provide insight into the electron-transfer kinetics at the electrode–electrolyte interface. Fig. 3c displays the Nyquist plots of the three electrodes recorded in the same electrolyte solution in 0.1 M KCl solution containing 2.5 mM $[Fe(CN)_6]^{3-/4-}$ over a frequency range of 0.01 kHz to 1000 kHz, with an excitation amplitude of 10 mV. Among the three evaluated electrodes, the bare SPE exhibited the largest semicircle in the high-frequency region, indicating a high charge transfer resistance. In contrast, Gd_2O_3/SPE showed a smaller semicircle, implying improved interfacial conductivity. Most notably, the Fe-doped Gd_2O_3/SPE showed the smallest semicircle, signifying a substantial reduction in charge transfer resistance and, consequently, enhanced electron transfer kinetics. The reduced R_{ct} in the Fe-doped Gd_2O_3/SPE is attributed to the incorporation of Fe into the Gd_2O_3 matrix, which likely facilitates faster electron transfer by lowering the interfacial energy barrier. According to the Randles equivalent circuit model and fitting results shown in Fig. S2, the R_{ct} values were found to be 1952 Ω for bare SPE, 820 Ω for Gd_2O_3/SPE, and 508 Ω for Fe-doped Gd_2O_3/SPE. These results confirm the marked improvement in electrical conductivity due to Fe doping. Furthermore, by using the calculated ECSA and R_{ct} values, the heterogeneous electron transfer rate constant (k^0) and the exchange current density (j_0) can be determined based on the two equations:[41,45]

$$k^0 = RT/n^2F^2ACR_{ct} \text{ and } j_0 = RT/nFAR_{ct}$$

here, R represents the universal gas constant (8.314 J mol^{-1} K^{-1}), T denotes the thermodynamic temperature (298.15 K), and F is the Faraday constant (96 485.33 C mol^{-1}). The Fe-doped Gd_2O_3/SPE demonstrated k^0 value of 10.63×10^{-7} cm s^{-1} and j_0 of 2.56×10^{-4} A cm^{-2} (Fig. 3d). These values were approximately 1.22 and 1.08 times higher, respectively, than those obtained for Gd_2O_3/SPE (8.70×10^{-7} cm s^{-1} and 2.10×10^{-4} A cm^{-2}). In comparison, the bare SPE exhibited the lowest values, with k^0 and j_0 measured at 4.35×10^{-7} cm s^{-1} and 1.05×10^{-4} A cm^{-2}, respectively. These findings underscore the significant role of Fe doping in enhancing interfacial electron transfer by both reducing R_{ct} and increasing k^0 and j_0, thus confirming the significant enhancement in electron transfer kinetics and the superior electrochemical performance of the Fe-doped Gd_2O_3/SPE electrode.

3.3. Electrochemical behavior and electrocatalytic activity of CAP at the bare SPE and Gd_2O_3-, Fe-doped Gd_2O_3-modified SPE electrodes

To elucidate the influence of Fe doping on the electronic conductivity and electrocatalytic activity of Fe-doped Gd_2O_3/SPE for the electrochemical detection of CAP, three electrochemical techniques including CV, LSV, and CA were used. Fig. 4a shows the CV curves of the bare SPE, Gd_2O_3/SPE, and Fe-doped Gd_2O_3/SPE in 0.1 M PBS (pH 7.4) containing 50 μM CAP a scan rate of 50 mV s^{-1}. As can be seen, an irreversible peak in the potential range from −0.75 V to −0.9 V was observed for all three unmodified and modified SPE electrodes. This peak is related to the irreversible reduction of the nitro group (R–NO_2) in a four-electron and four-proton process to the hydroxylamine group of aryl hydroxylamine (R–NHOH) in two steps:[46]

$$R\text{–}NO_2 + e^- \rightarrow R\text{–}NO_2^- \text{ (slow)}$$

$$R\text{–}NO_2^- + 3e^- + 4H^+ \rightarrow R\text{–}NHOH + H_2O \text{ (fast)}$$

The reduction peak current intensities of CAP for the bare SPE, Gd_2O_3/SPE, and Fe-doped Gd_2O_3/SPE are shown in Fig. 4b. For the bare SPE and Gd_2O_3/SPE, the modification of SPE with Gd_2O_3 NPs remarkably improved the CAP analytical sensing performance. The reduction peak current response of CAP recorded at Gd_2O_3/SPE (14.9 μA) was ∼1.48-fold higher than that of the bare SPE (10.1 μA). More interestingly, the proposed electrochemical sensing platform based on Fe-doped Gd_2O_3/SPE exhibits the highest response to CAP (17.9 μA), which are almost 1.2 and 1.8 times higher than that of the Gd_2O_3/SPE and the bare SPE, respectively. This result indicates that the incorporation of Fe atoms into the structure of Gd_2O_3 has the potential to be an effective way to improve the sensing performance of electrochemical sensors for the detection of CAP.

The influence of Fe doping on the electrochemical kinetics of CAP was further investigated by studying the effect of scan rate on the reduction peak current intensity. Fig. 4(c1), (d1) and (e1) illustrate the CV responses of 50 μM CAP in 0.1 M PBS (pH 7.4) solution on the bare SPE, Gd_2O_3/SPE, and Fe-doped Gd_2O_3/SPE with various scan rates ranging from 10 to 60 mV s^{-1}, respectively. It can be seen that at three investigated electrodes, the CAP reduction peak current intensities increased with the increasing of scan rate, demonstrating that the electrochemical reduction of CAP is the surface adsorption-controlled process.[26,47] This result is consistent with the electrochemical behavior of CAP in many previous studies. There is a good linear relationship between the reduction peak current intensities *vs.* scan rates, corresponding to the linear regression equations (Fig. 4(c2), (d2) and (e2)):

For SPE:

$$\Delta I_{pc}\ (\mu A) = 0.157\ (\text{mV s}^{-1}) + 0.782/R^2 = 0.997$$

For Gd_2O_3/SPE:

$$\Delta I_{pc}\ (\mu A) = 0.179\ (\text{mV s}^{-1}) + 4.494/R^2 = 0.997$$

For Fe-doped Gd_2O_3/SPE:

$$\Delta I_{pc}\ (\mu A) = 0.291\ (\text{mV s}^{-1}) + 0.949/R^2 = 0.999$$

Furthermore, the adsorption capacity (Γ) of CAP on the surface of the bare SPE, Gd_2O_3/SPE, and Fe-doped Gd_2O_3/SPE can ascertained by using the following equation:[3,26]

$$\Delta I_p = \frac{n^2F^2A\Gamma}{4RT}.$$

According to that equation, the calculated adsorption capacities of CAP at the bare SPE, Gd_2O_3/SPE, and Fe-doped Gd_2O_3/SPE were approximately 1.66×10^{-8}, 1.83×10^{-8}, and 2.77×10^{-8} mol cm^{-2}, respectively. This indicate that Fe doping promotes the generation of a larger number of active sites for

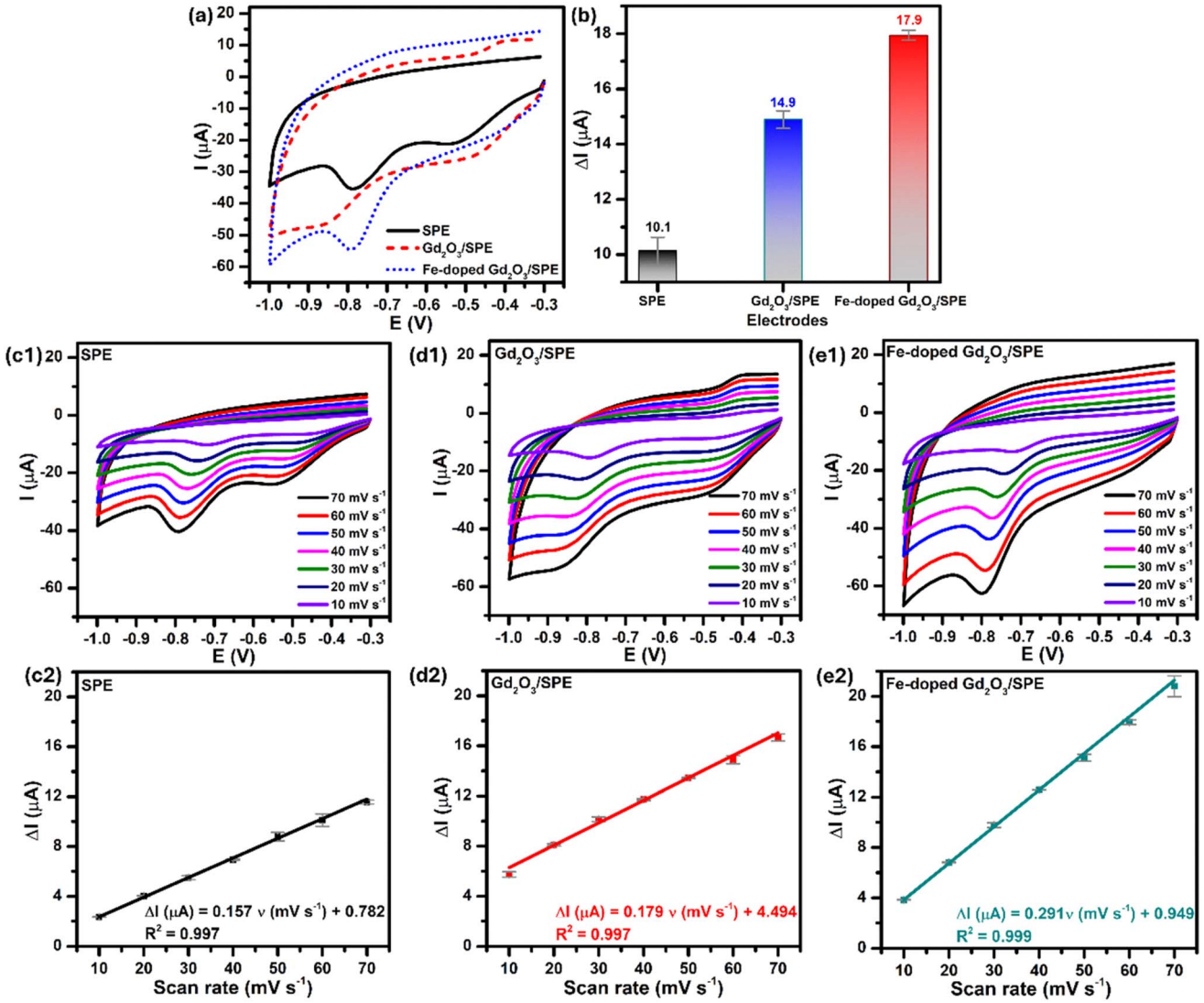

Fig. 4 (a) CV voltammograms and (b) the corresponding bar chart diagram of the reduction peak currents of the bare SPE, Gd_2O_3/SPE, and Fe-doped Gd_2O_3/SPE in 0.1 M PBS (pH 7.4) containing 50 μM CAP at a scan rate of 50 mV s^{-1}; CV voltammograms in 0.1 M PBS (pH 7.4) containing 50 μM CAP at different scan rates from 10 to 70 mV s^{-1} and the calibration plots of reduction peak currents against scan rate of the bare SPE (c1 and c2), Gd_2O_3/SPE (d1 and d2), and Fe-doped Gd_2O_3/SPE (e1 and e2).

capturing CAP molecules, resulting in superior electrochemical sensing activity as compared to the bare SPE and undoped Gd_2O_3 modified electrodes.

The electrocatalytic activity of the bare SPE, undoped Gd_2O_3-, and Fe-doped Gd_2O_3-modified electrodes for the electro-oxidation of CAP was investigated by using the LSV and CA measurements. Fig. 5a illustrates the LSV curves of the bare SPE, Gd_2O_3/SPE, and Fe-doped Gd_2O_3/SPE in 0.1 M PBS (pH 7.4) containing 50 μM CAP. By extrapolating a linear fit from a selected region of the LSV curves, the onset potential (E_{onset}) values for the bare SPE, Gd_2O_3/SPE, and Fe-doped Gd_2O_3/SPE were found to be −0.71, −0.68, and −0.4 V, respectively. The Fe-doped Gd_2O_3/SPE demonstrated a negative shift in the E_{onset} value of about 310 and 280 mV compared to that of the bare SPE and undoped Gd_2O_3-modified electrode, respectively. In general, a more positive onset potential in the negative potential region ($E < 0$ V) indicates higher electrocatalytic activity and fast reaction kinetics.[48,49] With Fe doping, not only the E_{onset} value shifted significantly to a more positive potential but also an increase in the electro-reduction peak current response were observed. As shown in Fig. 5b, the reduction peak current intensity of the Fe-doped Gd_2O_3-modified electrodes were calculated to be about 27.8 μA. This value was 3.0 and 1.96 times greater than that of the bare SPE and undoped Gd_2O_3-modified electrode, respectively. Furthermore, the Tafel plots were constructed by fitting the polarization curve, *i.e.*, potential (V) *vs.* the logarithm of absolute value of current density ($\log|I|$). Inset Fig. 5b illustrates the Tafel plots of the bare SPE, Gd_2O_3/SPE, and Fe-doped Gd_2O_3/SPE, indicating that the Fe-doped Gd_2O_3/SPE has smaller Tafel slope and thus more favorable and more efficient CAP electro-reduction kinetics than the bare SPE and undoped Gd_2O_3-modified electrode.

The catalytic rate constant (k_{cat}) values for the electro-reduction between CAP and the bare SPE, Gd_2O_3/SPE, and Fe-

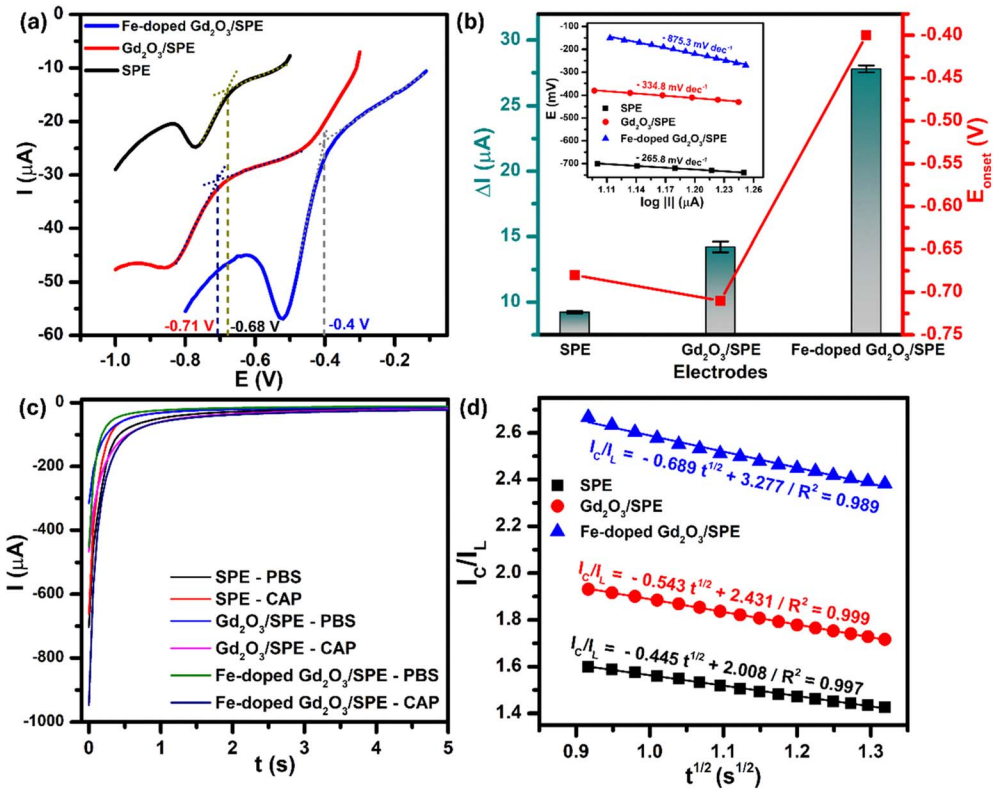

Fig. 5 (a) LSV curves and (b) the corresponding bar chart diagram of the reduction peak currents and the onset potentials of CAP recorded on the bare SPE, Gd_2O_3/SPE, and Fe-doped Gd_2O_3/SPE in 0.1 M PBS (pH 7.4) containing 50 μM CAP. (c) Chronoamperometric response of the bare SPE, Gd_2O_3/SPE, and Fe-doped Gd_2O_3/SPE in 0.1 M PBS (pH 7.4) and 0.1 M PBS (pH 7.4) containing 50 μM CAP and (d) the plot of I_C/I_L *vs.* $t^{1/2}$ acquired from the chronoamperograms.

doped Gd_2O_3/SPE can be also determined by using CA technique, according to the Galus method:[42] $I_C/I_L = \pi^{1/2}(k_{cat}C_b t)^{1/2}$. Where I_C and I_L are the catalytic current in the absence and presence of CAP, respectively, C_b the bulk concentration of CAP (mol cm^{-3}), t is the elapsed time (s). Fig. 5c shows chronoamperograms recorded at the bare SPE, undoped Gd_2O_3-, and Fe-doped Gd_2O_3-modified electrodes in 0.1 M PBS (pH 7.4) and 0.1 M PBS (pH 7.4) containing 50 μM CAP. As can be seen in Fig. 5d, the ratio of catalytic current to blank current (I_C/I_L) was linearly dependent on the square root of time ($t^{1/2}$) with the regression equations can be expressed as follows:

For SPE:

$$I_C/I_L = -0.045t^{1/2} + 2.008/R^2 = 0.997$$

For Gd_2O_3/SPE:

$$I_C/I_L = -0.543t^{1/2} + 2.431/R^2 = 0.999$$

For Fe-doped Gd_2O_3/SPE:

$$I_C/I_L = -0.689t^{1/2} + 3.277/R^2 = 0.989$$

As a result, from the slopes of the I_C/I_L against $t^{1/2}$ plot, the k_{cat} values for the bare SPE, Gd_2O_3/SPE, and Fe-doped Gd_2O_3/SPE are calculated to be 0.63×10^{-3}, 0.93×10^{-4}, and 1.5×10^{-4} M^{-1} s^{-1}, respectively. The k_{cat} value of Fe-doped Gd_2O_3-modified electrode was 2.38- and 1.61-fold higher than the bare SPE and undoped Gd_2O_3-modified electrode, further indicating superior electrocatalytic activity toward the electro-reduction of CAP.

3.4. Discussions

The electrochemical kinetic for the $[Fe(CN)_6]^{3-/4-}$ redox system and the analytical sensing performance for the CAP electroreduction of the bare SPE, Gd_2O_3/SPE, and Fe-doped Gd_2O_3/SPE were summarized in Table 1. Overall, the incorporation of Fe ions into the Gd_2O_3 nanostructures plays a crucial role in enhancing electrochemical performance, as evidenced by the fact that the Fe-doped Gd_2O_3/SPE significantly outperforms both bare SPE and undoped Gd_2O_3/SPE in nearly all key electrochemical kinetic parameters. CV and EIS analyses using the $[Fe(CN)_6]^{3-/4-}$ redox probe consistently demonstrate that Fe doping significantly improves the electrochemical properties of Gd_2O_3/SPE. These enhancements are evidenced by increased redox peak currents, significantly reduced charge transfer resistance, higher electron transfer rates, elevated heterogeneous electron transfer rate constants, and greater exchange current densities. In terms of CAP sensing, the Fe-doped Gd_2O_3/SPE also demonstrates the highest sensing performance among the tested electrodes, as validated by CV, LSV, and CA analyses. By incorporating Fe atom into the structure of Gd_2O_3 NPs, the Fe-doped Gd_2O_3/SPE exhibited excellent adsorption performance and electrocatalytic activity. These improvements are reflected in the increased adsorption capacity, a positive shift in the onset potential in the

Table 1 The electrochemical kinetic parameters of the bare SPE, Gd_2O_3/SPE, and Fe-doped Gd_2O_3/SPE in $[Fe(CN)_6]^{3-/4-}$ redox probe and CAP antibiotic

	SPE	Gd_2O_3	Fe-doped Gd_2O_3
Analyte: $[Fe(CN)_6]^{3-/4-}$			
Anodic peak current (ΔI_{pa}, μA)	56.6	77.0	81.4
Cathodic peak current (ΔI_{pc}, μA)	51.2	77.2	86.4
Electrochemically active surface area (ECSA, cm^2)	0.126	0.149	0.197
Charge-transfer resistance (R_{ct}, Ω)	1952	820.4	508
Heterogeneous electron-transfer rate constant (k^0, $\times 10^{-7}$ cm s^{-1})	4.35	8.70	10.63
Exchange current density (j_0, $\times 10^{-4}$ A cm^{-2})	1.05	2.10	2.56
Analyte: CAP			
Reduction peak current – CV (μA)	10.1	14.9	17.9
Adsorption capacity (Γ, $\times 10^{-8}$ mol cm^{-2})	1.66	1.83	2.77
E_{onset} (V)	−0.71	−0.68	−0.4
Reduction peak current – LSV (μA)	9.2	14.2	27.8
Catalytic rate constant (k_{cat}, $\times 10^4$ M^{-1} s^{-1})	0.63	0.93	1.5

negative potential region, higher electro-reduction peak current response, and smaller Tafel slope.

These notable enhancements in electrochemical kinetic parameters for the $[Fe(CN)_6]^{3-/4-}$ redox system and CAP electro-reduction are attributed to the synergistic effect between improved electrical conductivity and enhanced electro-catalytic activity introduced by Fe doping. The incorporation of Fe-doped Gd_2O_3 NPs enhances the electronic conductivity of the electrode, thereby providing a more direct and shorter electron-transfer pathway and facilitating charge transfer. Specifically, while the Gd_2O_3/SPE reduced R_{ct} by 2.4 times compared to the bare SPE, the Fe-doped Gd_2O_3/SPE showed a much more significant 3.8-fold reduction. Consequently, the k^0 and j_0 values of the Fe-doped Gd_2O_3/SPE were 2.4 times higher than those of the bare SPE and 1.2 times higher than the Gd_2O_3/SPE. Furthermore, the Fe-doped Gd_2O_3 NPs creates extensive active interfaces and strengthens the interaction between the catalytically active areas and the analyte, ultimately resulting in higher CAP adsorption capacity. The calculated results show that Fe-doped Gd_2O_3 exhibits the highest ECSA and Γ values (0.197 cm^2 and 2.77 $\times 10^{-8}$ mol cm^{-2}). These values represent a 1.56 and 1.67-fold increase over the bare SPE, and a 1.32 and 1.51-fold improvement compared to the undoped Gd_2O_3/SPE, respectively. Additionally, the pronounced electrocatalytic effect of the Fe-doped Gd_2O_3 NPs lowers the activation energy barrier, thereby not only accelerating the CAP reduction reaction kinetics but also facilitating the occurrence of electrochemical processes under milder conditions. This is quantitatively confirmed by the k_{cat} values, which rises from 0.63 $\times 10^4$ (bare SPE) to 0.93 $\times$ 10^4 (Gd_2O_3/SPE), reaching a maximum of 1.5 $\times$ 10^4 M^{-1} s^{-1} for the Fe-doped Gd_2O_3/SPE. Overall, these synergistic effects contribute to a substantial improvement in analytical sensing performance, making Fe-doped Gd_2O_3/SPE a highly effective nanoplatform for CAP detection.

3.5. Optimization of electrochemical parameters

The electrochemical behavior of CAP is significantly influenced by the pH of the supporting electrolyte, owing to the role of protons in the electrochemical reaction. To establish the optimal pH conditions for CAP electro-oxidation using a Fe-doped Gd_2O_3/SPE, differential pulse voltammetry (DPV) was performed across a broad pH range, from acidic to basic environments. As depicted in Fig. 6a, increasing the pH from 3.0 to 8.0 induced a gradual negative shift in the oxidation peak potential of CAP, indicating the participation of protons in the electrode reaction. The dependencies of peak current and peak potential on pH are summarized in Fig. 6b, with the black curve representing peak current and the red curve representing peak potential. Notably, the CAP reduction peak current intensities increased as pH rose from 3 to 6, suggesting enhanced electron transfer efficiency under mildly acidic conditions. However, further increases in pH beyond 6 led to a decline in current response, implying diminished electrochemical activity in more alkaline conditions. These observations identify pH 6 as the optimal condition for CAP detection. Furthermore, the oxidation peak potential exhibited a linear correlation with pH over the tested range, as expressed by the regression equation: E_{pc} (V) = −0.003 pH − 0.445. The slope of −0.030 V pH^{-1} unit is not close to the theoretical Nernstian value (−0.059 V pH^{-1}), suggesting the irreversible nature of electrochemical reduction reaction of CAP.[3,9,26] Considering that the CAP reduction involves a four-electron process, it is inferred that four protons are also involved. This proposed mechanism is consistent with previously reported electrochemical pathways,[3,9,26] as illustrated in Fig. 6c.

In addition to pH optimization, the influence of accumulation time from 60 to 180 s was also investigated (Fig. 6d). As shown in Fig. 6e, the peak current increased with longer accumulation times, reaching a maximum at 150 s. Beyond this point, a decline was observed. This is likely due to saturation of the electrode surface. Thus, an accumulation time of 150 s was determined to be optimal for subsequent electrochemical measurements.

3.6. Electrochemical determination of CAP at Gd_2O_3- and Fe-doped Gd_2O_3-modified SPE electrodes

Under all the optimized experimental conditions, the electrochemical sensing performance of the proposed undoped Gd_2O_3-

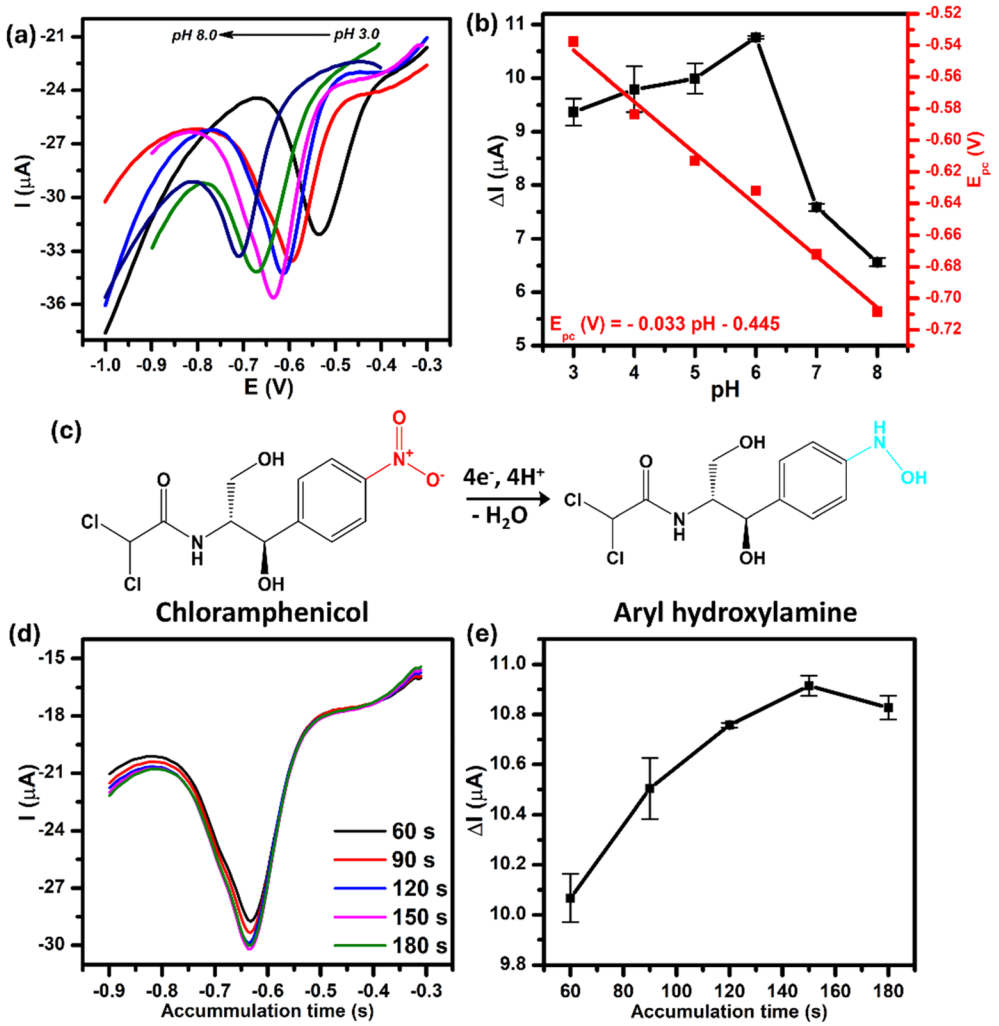

Fig. 6 (a) DPV voltammograms of Fe-doped Gd_2O_3/SPE in 0.1 M PBS containing 50 μM CAP at various pH values from 3.0 to 8.0 and (b) the corresponding calibration plots of reduction peak current and reduction peak potential of CAP against pH values with error bars; (c) the electrochemical reduction mechanism of CAP; (d) DPV voltammograms and (e) the corresponding calibration plots of reduction peak currents of 50 μM CAP recorded at Fe-doped Gd_2O_3/SPE with various accumulation time.

and Fe-doped Gd_2O_3-modified electrodes towards the CAP determination was investigated by DPV technique. Fig. 7a and c illustrate DPV responses of the Gd_2O_3/SPE and Fe-doped Gd_2O_3/SPE in 0.1 M PBS (pH 6.0) containing different concentrations of CAP, respectively. As can be observed, on increasing the concentration of CAP, the electro-reduction peak current intensity was found to increase in both cases. The Gd_2O_3/SPE exhibited a linear response across a concentration range from 2.5 to 100 μM with linear regression equation can be expressed as: ΔI_{pc} (μA) = $0.123C_{CAP}$ (μM) + 0.172, R^2 = 0.998 (Fig. 7b). Compared to undoped Gd_2O_3-modified electrode, the remarkable enhancement in electronic conductivity and electrocatalytic activity of Fe-doped Gd_2O_3/SPE led to an extraordinary analytical performance with wider dynamic linear range. Namely, with the incorporation of Fe as a dopant in the Gd_2O_3 NPs, the electro-reduction peak current intensity on Fe-doped Gd_2O_3/SPE increased linearly with rising CAP concentration range from 0.5 to 100 μM. Regression correlation is as follow: ΔI_{pc} (μA) = $0.199C_{CAP}$ (μM) + 0.361 with a high correlation coefficient of $R^2 = 0.994$ (Fig. 7d). From the obtained slope value from linear regression and electrochemical active surface area (ECSA) value, the electrochemical sensitivity values of the Gd_2O_3/SPE and Fe-doped Gd_2O_3/SPE were calculated to be about 0.825 and 1.010 μA μM^{-1} cm^{-2}, respectively. The limit of detection (LOD) was calculated using the IUPAC formula LOD = $3S_b/m$, where S_b represents the standard deviation of ten replicate blank measurements, and m stands for the slope of the calibration curve. According to that equation, the detection limit of the Gd_2O_3/SPE and Fe-doped Gd_2O_3/SPE for the detection of CAP were determined to be 1.17 and 0.25 μM, respectively.

The analytical sensing performance of the Fe-doped Gd_2O_3-modified electrode for the detection of CAP was systematically evaluated and compared with previously reported sensing platforms, with the corresponding analytical parameters were summarized in Table 2. The proposed electrochemical sensor based on Fe-doped Gd_2O_3 NPs offers several distinctive advantages. First, the proposed sensing platform is based on a single-

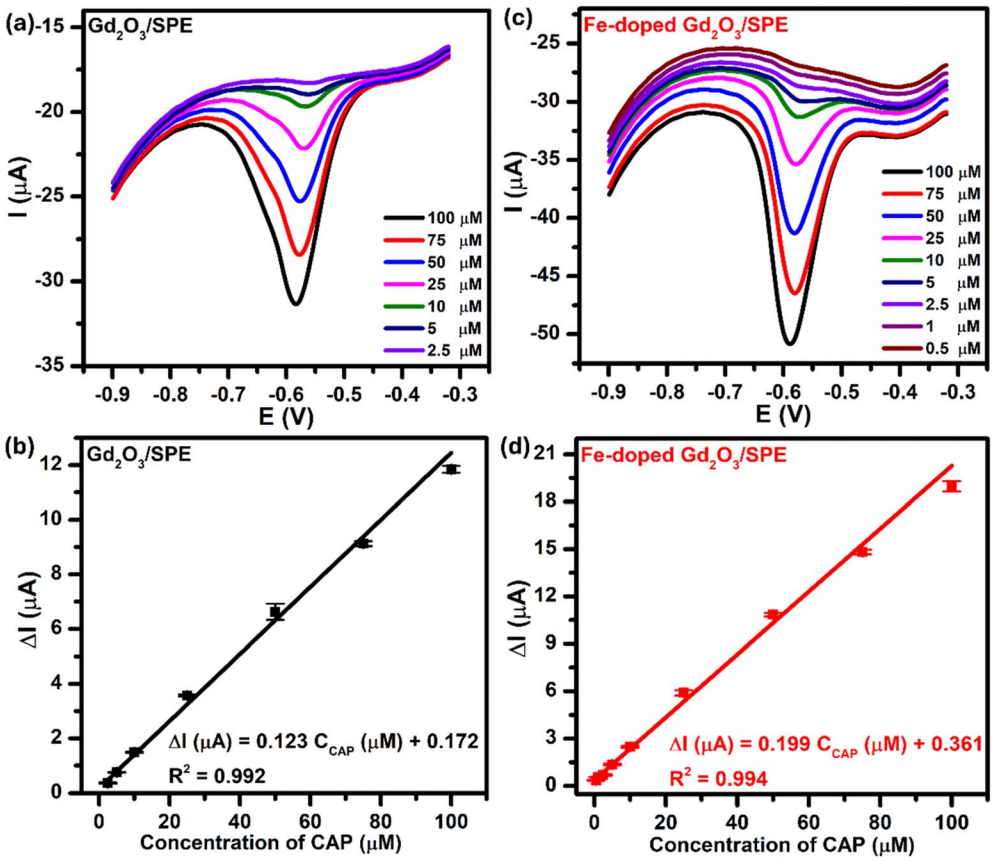

Fig. 7 DPV voltammograms recorded in 0.1 M PBS (pH 6.0) solution containing different CAP concentrations from 0.5 to 100 μM and the calibration plots between reduction peak current responses *vs.* various concentrations of CAP of Gd_2O_3/SPE (a and b) and Fe-doped Gd_2O_3/SPE (c and d).

component doped rare-earth oxide without the need for noble metals, carbon nanomaterials, or complex heterostructures, thereby reducing material cost and fabrication complexity. Second, the synthesis and electrode modification processes are straightforward, involving a facile thermal decomposition method followed by simple drop-casting onto SPE, which is highly compatible with on-site applications. Finally, the Fe-doped Gd_2O_3/SPE exhibits a wide linear detection range, a low detection limit, and good practical applicability in pharmaceutical formulations and milk samples (as demonstrated below), demonstrating analytical capabilities that are comparable to or better than those of other modified electrodes. These results highlight the great potential of Fe-doped Gd_2O_3 NPs as a robust and efficient electrode material for the development of high-performance electrochemical sensors towards CAP detection and other toxic analytes.

3.7. Anti-interference ability, repeatability, feasibility, and storage stability studies of the proposed Fe-doped Gd_2O_3-based electrochemical sensor

In real-world conditions, the presence of metal ions, organic compounds, and antibiotics can potentially interfere with the analysis of CAP and lead to inconsistent analytical results. Therefore, attaining robust anti-interference ability is essential for ensuring the accurate electrochemical determination of CAP and enhancing the overall sensing performance of the proposed sensor. Therefore, the anti-interference ability of the Fe-doped Gd_2O_3/SPE were conducted by measuring the DPV reduction peak current response of 50 μM CAP in the presence of 20-fold concentrations of possible interfering ions (K^+, Cu^{2+}, Ni^{2+}, Zn^{2+}, and Fe^{3+}), co-interfering organic compounds (4-nitrophenol, ascorbic acid, and glucose), and antibiotics (paracetamol, azithromycin, erythromycin, and furazolidone), as shown in Fig. 8a. It can be observed that the presence of potential interfering substances induced only minor fluctuations in the background current without generating any noticeable interference peaks within the potential range of −0.9 to −0.3 V. As illustrated in Fig. 8b, the relative errors – calculated by dividing the absolute error of ΔI_{pc} value of 50 μM CAP in the presence of the interferers by the measured ΔI_{pc} value of 50 μM CAP, remained below 11%. These results demonstrate that the proposed electrochemical sensor based on Fe-doped Gd_2O_3 NPs possesses excellent anti-interference capability, ensuring reliable and accurate detection of CAP under complex sample conditions.

The electrochemical repeatability of the developed sensor was also scrutinized by conducting 10 consecutive repeated DPV measurements using 0.1 M PBS containing 50 μM CAP under the same conditions (Fig. 8c). The electro-reduction peak current intensities were extracted and presented in Fig. 8d. The Fe-doped Gd_2O_3-modified electrode maintained stable

Table 2 Comparative study of the performance of various modified electrodes for CAP electrochemical detection[a]

Modified electrodes	Techniques	Analytical ranges (μM)	Limit of detection (μM)	Sensitivity (μA μM^{-1} cm^{-2})	Real samples	Ref.
CuNPs@CNTs/MIP/GCE	CV	10–500	10.0	—	Milk	50
Co3O4@rGO/GCE	DPV	2–2000	1.16	0.42	Milk	51
AuNPs–N doped graphene/GCE	LSV	2–80	0.59	—	Eye drops	52
CuO/SPE	DPV	2.5–50	0.45	0.43	Milk Honey	9
AuNPs–GO/GCE	Amperometry	1.5–2.95	0.25	3.81	Milk Honey Eye drops	53
CuNPs-MoS_2/SPE	DPV	0.5–50	0.19	0.54	Milk Honey	9
Ag–Cu_2O/SPE	DPV	0.5–150	0.16	1.64	—	3
Sr–ZnO@rGO/SPE	LSV	0.19–410.84	0.131	1.06	Milk Powdered milk	54
Fe-doped Gd_2O_3/SPE	DPV	0.5–100	0.25	1.01	Pharmaceutical formulations milk	This work

[a] GCE: glassy carbon electrode; MIP: molecularly imprinted polymer CNTs: single-walled carbon nanotubes; rGO: reduced graphene oxide; GO: graphene oxide.

reduction responses of CAP in 10 consecutive DPV measurements, with the relative standard deviation (RSD) value of 0.89%, which highlights its outstanding repeatability and robustness for electrochemical detection of CAP.

The storage stability of the Fe-doped Gd_2O_3/SPE was evaluated *via* DPV analysis of 50 μM CAP before storage, after 1 day and after 4 days. The results indicate that although a minor shift in the reduction potential was observed after 4 days, the

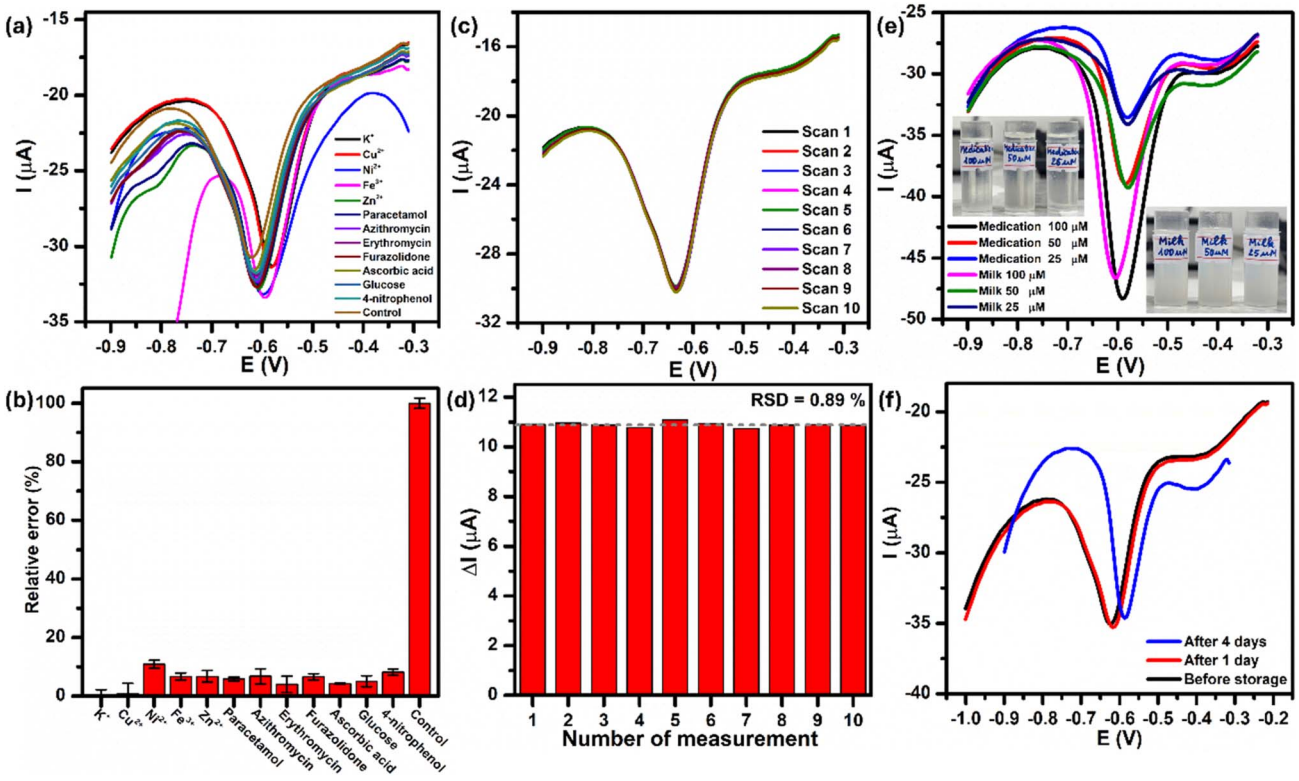

Fig. 8 (a and b) Interference investigation of Fe-doped Gd_2O_3/SPE in 0.1 M PBS solution containing 50 μM CAP with 20-fold concentration of interference substances; (c and d) the repeatability performance of Fe-doped Gd_2O_3/SPE for 10 consecutive measurements in 0.1 M PBS solution containing 50 μM CAP; (e) DPV voltammograms for the determination of CAP in three milk and pharmaceutical samples (25, 50, and 100 μM) using Fe-doped Gd_2O_3/SPE and (f) the storage stability at the different storage periods between 4 days. Inset (e): image of spiked milk and pharmaceutical samples containing different concentrations of CAP.

Table 3 Electrochemical detection of CAP in the commercial pharmaceutical tablet and milk samples using Fe-doped Gd_2O_3-modified electrode

Real sample	Labeled values (μM)[a]	Found values (μM)	Recovery (%)	RSD (%)
Phamaceutical tablet	100	102.3	102.3	2.1
	50	52.0	104.0	2.0
	25	28.5	114.0	3.5
Real sample	Spiked values (μM)[a]	Found values (μM)	Recovery (%)	RSD (%)
Milk	150	97.1	97.1	2.0
	50	47.1	94.1	0.4
	25	25.7	102.8	0.6

[a] Each sample was assayed in triplicate ($n = 3$).

reduction peak current (10.73 μA) remained stable compared with the initial measurement (10.45 μA) and the 1-day counterpart (10.47 μA), demonstrating the good operational stability of the proposed electrochemical sensor.

To evaluate the practical applicability of the developed electrochemical sensing platform, the Fe-doped Gd_2O_3-modified electrode was employed for the determination of CAP concentrations in commercial pharmaceutical tablet and milk samples, as illustrated in Fig. 8e and f. The recovery and RSD values were measured, and the results are shown in Table 3. The milk samples spiked with different CAP concentrations (25, 50, and 100 μM) showed a recovery value of 25.7–97.1 μM with RSD values below 2.0%. For the pharmaceutical tablet samples, the mean recoveries were in the range of 102.3 and 114.0% with the RSD values ranging from 2.0 to 3.5%. These obtained results indicate that the developed electrochemical sensing platform based on Fe-doped Gd_2O_3 NPs can serves as a reliable and effective method for the quantitative analysis of CAP in pharmaceutical formulations and milk samples.

4. Conclusions

In summary, we have successfully developed an electrochemical sensing nanoplatform based on Fe-doped Gd_2O_3 NPs for the sensitive and selective detection of CAP. As compared to the bare SPE and undoped Gd_2O_3-modified electrode, the Fe-doped Gd_2O_3/SPE exhibits excellent analytical sensing performance towards the CAP detection, featuring satisfactory repeatability, high anti-interference ability. Through optimizing the detection conditions, the Fe-doped Gd_2O_3-modified electrode could detect CAP in a wide linear dynamic range from 0.5 to 100 μM with a high electrochemical sensitivity of 1.010 μA μM^{-1} cm^{-2} and a low detection limit of 0.25 μM. The outstanding analytical performance of the Fe-doped Gd_2O_3/SPE can be attributed to the synergistic enhancement of electronic conductivity and electrocatalytic ability. The presence of Fe ions as dopants leads to a significant increase in the electrochemically active surface area and the adsorption capacity for target analytes, which collectively accelerate electron transfer kinetic and provide more active sites for electrochemical reactions. Additionally, by modifying the electronic structure of Gd_2O_3, Fe ions accelerate the electrocatalytic activity, thus lowering the activation energy required for the electrochemical reduction of CAP. Moreover, the proposed Fe-doped Gd_2O_3/SPE sensor illustrated effective detection of CAP in pharmaceutical formulations and milk samples. These intriguing results indicated that the electrochemical sensing platform based on Fe-doped Gd_2O_3 NPs has great promise for on-site and point-of-care analytical applications, particularly in the quality control of pharmaceutical formulations and the detection of antibiotic residues in food products.

Author contributions

T.-A. Nguyen: conceptualization, methodology, data curation, validation, investigation, writing-original draft; N. H. A. Nguyen: formal analysis, writing – original draft; N. X. Dinh: conceptualization, formal analysis; L. T. T. Tam: validation, investigation, formal analysis; N. X. Quang: validation, formal analysis; L. T. Lu: methodology, formal analysis, writing-review & editing; M.-H. Phan: conceptualization, supervision, writing-review & editing; A.-T. Le: conceptualization, supervision, project administration, writing-review & editing.

Conflicts of interest

The authors declare that they have no known competing financial interests or personal relationships that could have appeared to influence the work reported in this paper.

Data availability

The authors confirm that all the data supporting the findings of this study are available within the article and its supplementary information (SI). Supplementary information: CV and EIS results. See DOI: https://doi.org/10.1039/d5ra09035k.

Acknowledgements

This research is funded by the Phenikaa University under grant PU2023-1-A-21. The authors would like to acknowledge the support for Electrochemical measurements from NEB Lab (Phenikaa University) and SEM supports from IOP-VAST and XRD from VNU-Hanoi.

References

1 R. Keçili, S. Büyüktiryaki and C. M. Hussain, *TrAC, Trends Anal. Chem.*, 2019, **110**, 259–276.
2 V. D. Krishna, K. Wu, D. Su, M. C. J. Cheeran, J.-P. Wang and A. Perez, *Food Microbiol.*, 2018, **75**, 47–54.
3 T.-A. Nguyen, H. A. Tu, P. T. L. Huong, V. H. Ong, P. D. Thang, N. Q. Hoa, N. X. Dinh and A.-T. Le, *Electrochim. Acta*, 2025, 146472.
4 R. Umapathi, S. M. Ghoreishian, S. Sonwal, G. M. Rani and Y. S. Huh, *Coord. Chem. Rev.*, 2022, **453**, 214305.
5 N. T. Anh, N. Van Quy, O. Van Hoang, N. X. Dinh and A.-T. Le, *Nanoscale Adv.*, 2024, **6**, 256–267.
6 H. Teymourian, M. Parrilla, J. R. Sempionatto, N. F. Montiel, A. Barfidokht, R. Van Echelpoel, K. De Wael and J. Wang, *ACS Sens.*, 2020, **5**, 2679–2700.
7 K. Beaver, A. Dantanarayana and S. D. Minteer, *J. Phys. Chem. B*, 2021, **125**, 11820–11834.
8 C. Zhu, G. Yang, H. Li, D. Du and Y. Lin, *Anal. Chem.*, 2015, **87**, 230–249.
9 N. T. Anh, N. X. Dinh, T. N. Pham, L. K. Vinh, L. M. Tung and A.-T. Le, *RSC Adv.*, 2021, **11**, 30544–30559.
10 L. Jiao, W. Xu, Y. Wu, H. Wang, L. Hu, W. Gu and C. Zhu, *Anal. Chem.*, 2023, **95**, 433–443.
11 N. T. Anh, N. X. Dinh, N. N. Huyen, P. T. L. Huong, V. N. Phan, P. D. Thang, H. Van Tuan, T. Van Tan and A.-T. Le, *J. Electrochem. Soc.*, 2023, **170**, 17510.
12 J. M. George, A. Antony and B. Mathew, *Microchim. Acta*, 2018, **185**, 1–26.
13 J. Li, L. Sun, X. Wang, L. Li, Q. Zhu, B. Ouyang, E. Kan and W. Zhang, *Chem. Eng. J.*, 2022, **433**, 134597.
14 S. Majeed and S. A. Shivashankar, *J. Mater. Chem. B*, 2014, **2**, 5585–5593.
15 S. Das, A. Chakravorty, S. Luktuke, A. Raj, A. A. Mini, K. Ramesh, A. N. Grace, S. K. Pandey and V. Raghavan, *Results Chem.*, 2023, **6**, 101189.
16 Q.-Q. Xu, X.-L. Cheng, B.-Y. Zhang, F. Zhang, X. Wang, S.-S. Li and Y.-X. Zhang, *Anal. Chim. Acta*, 2022, **1232**, 340472.
17 P. Phonsuksawang, P. Khajondetchairit, T. Butburee, S. Sattayaporn, N. Chanlek, P. Hirunsit, S. Suthirakun and T. Siritanon, *Electrochim. Acta*, 2020, **340**, 135939.
18 M.-A. Ha, S. M. Alia, A. G. Norman and E. M. Miller, *ACS Catal.*, 2024, **14**, 17347–17359.
19 S. J. Malode, N. Navada, M. M. Shanbhag, N. P. Shetti, A. N. Alodhayb, K. E. Alzahrani, H. Albrithen and A. K. Assaifan, *Microchem. J.*, 2024, **207**, 111655.
20 N. Lavanya, C. Sekar, S. Ficarra, E. Tellone, A. Bonavita, S. G. Leonardi and G. Neri, *Mater. Sci. Eng. C*, 2016, **62**, 53–60.
21 Y. Shao, Y. Wang, Y. Yuan and Y. Xie, *Sci. Total Environ.*, 2021, **798**, 149205.
22 B. Singh, A. Bhat and K. Ravi, *Environ. Health*, 2024, **2**, 618–622.
23 M. R. Siddiqui, Z. A. AlOthman and N. Rahman, *Arab. J. Chem.*, 2017, **10**, S1409–S1421.
24 Y. Ben, M. Hu, F. Zhong, E. Du, Y. Li, H. Zhang, C. B. Andrews and C. Zheng, *Environ. Res.*, 2022, **212**, 113387.
25 H. M. J. Feder, C. Osier and E. G. Maderazo, *Rev. Infect. Dis.*, 1981, **3**, 479–491.
26 N. N. Huyen, N. T. Anh, T. L. H. Phung, N. X. Dinh, N. T. Vinh, T. T. Loan, V. Q. Nguyen, D. L. Vu, L. M. Tung and A.-T. Le, *J. Electrochem. Soc.*, 2022, **169**, 106517.
27 Animal Medicinal Drug Use Clarification Act of 1994 (AMDUCA), FDA Title 21, 1994, 397.
28 EFSA Panel on Contaminants in the Food Chain (CONTAM), Scientific Opinion on Chloramphenicol in food and feed, *EFSA J.*, 2014, **12**, 3907.
29 L. T. T. Tam, N. T. N. Linh, L. T. Tam, D. V Thiet, P. H. Nam, N. T. H. Hoa, L. A. Tuan, N. T. Dung and L. T. Lu, *Mater. Adv.*, 2025, **6**, 1319–1329.
30 S. K. S. Patel, P. Dhak, M.-K. Kim, J.-H. Lee, M. Kim and S.-K. Kim, *J. Magn. Magn. Mater.*, 2016, **403**, 155–160.
31 B. J. Sarkar, J. Mandal, M. Dalal, A. Bandyopadhyay, B. Satpati and P. K. Chakrabarti, *J. Electron. Mater.*, 2018, **47**, 1768–1779.
32 D. Barreca, A. Gasparotto, A. Milanov, E. Tondello, A. Devi and R. A. Fischer, *Surf. Sci. Spectra*, 2007, **14**, 60–67.
33 N. Ullah, M. Imran, K. Liang, C.-Z. Yuan, A. Zeb, N. Jiang, U. Y. Qazi, S. Sahar and A.-W. Xu, *Nanoscale*, 2017, **9**, 13800–13807.
34 E. Külah, L. Marot, R. Steiner, A. Romanyuk, T. A. Jung, A. Wäckerlin and E. Meyer, *Sci. Rep.*, 2017, **7**, 43369.
35 G. Vijayaprasath, I. Habibulla, V. Dharuman, S. Balasubramanian and R. Ganesan, *ACS Omega*, 2020, **5**, 17892–17899.
36 T. Yamashita and P. Hayes, *Appl. Surf. Sci.*, 2008, **254**, 2441–2449.
37 N. S. McIntyre and D. G. Zetaruk, *Anal. Chem.*, 1977, **49**, 1521–1529.
38 S. Poulin, R. França, L. Moreau-Bélanger and E. Sacher, *J. Phys. Chem. C*, 2010, **114**, 10711–10718.
39 D. Wilson and M. A. Langell, *Appl. Surf. Sci.*, 2014, **303**, 6–13.
40 Z. Hou, P. Yan, B. Sun, H. Elshekh and B. Yan, *Results Phys.*, 2019, **14**, 102498.
41 T.-A. Nguyen, N. T. Loan, M. T. N. Pham, P. D. Thang, V. N. Phan, N. X. Dinh, T. Van Manh, V. H. Ong, V. D. Lam and A.-T. Le, *RSC Adv.*, 2024, **14**, 34471–34485.
42 A. J. Bard, L. R. Faulkner and H. S. White, *Electrochemical Methods: Fundamentals and Applications*, John Wiley & Sons, 2022.
43 C. Wei, S. Sun, D. Mandler, X. Wang, S. Z. Qiao and Z. J. Xu, *Chem. Soc. Rev.*, 2019, **48**, 2518–2534.
44 H. Ren, Y. Pan, C. C. Sorrell and H. Du, *J. Mater. Chem. A Mater.*, 2020, **8**, 3154–3159.
45 N. T. Anh, L. M. Tung, L. K. Vinh, N. Van Quy, O. Van Hoang, N. X. Dinh and A.-T. Le, *Nanoscale Adv*, 2024, **6**, 256–267.
46 Y. Ni, L. Wang and S. Kokot, *Anal. Chim. Acta*, 2001, **431**, 101–113.
47 N. T. Anh, N. X. Dinh, T. N. Pham, L. K. Vinh, L. M. Tung and A.-T. Le, *RSC Adv.*, 2021, **11**, 30544–30559.

48 E. E. Abdel-Hady, A. Gamal, H. Hamdy, M. Shaban, M. O. Abdel-Hamed, M. A. Mohammed and W. M. Mohammed, *Sci. Rep.*, 2023, **13**, 4870.
49 C. Batchelor-McAuley, *Curr. Opin. Electrochem.*, 2023, **37**, 101176.
50 A. Munawar, M. A. Tahir, A. Shaheen, P. A. Lieberzeit, W. S. Khan and S. Z. Bajwa, *J. Hazard. Mater.*, 2018, **342**, 96–106.
51 M. Yadav, V. Ganesan, R. Gupta, D. K. Yadav and P. K. Sonkar, *Microchem. J.*, 2019, **146**, 881–887.
52 J. Borowiec, R. Wang, L. Zhu and J. Zhang, *Electrochim. Acta*, 2013, **99**, 138–144.
53 R. Karthik, M. Govindasamy, S. M. Chen, V. Mani, B. S. Lou, R. Devasenathipathy, Y. S. Hou and A. Elangovan, *J. Colloid Interface Sci.*, 2016, **475**, 46–56.
54 S. V. Selvi, N. Nataraj and S. M. Chen, *Microchem. J.*, 2020, **159**, 105580.